Journal of Materials Chemistry A

Following the In-plane Disorder of Sodiated Hard Carbon through Operando Total Scattering

Journal:	*Journal of Materials Chemistry A*
Manuscript ID	TA-ART-03-2019-002413.R1
Article Type:	Paper
Date Submitted by the Author:	10-Apr-2019
Complete List of Authors:	Mathiesen , Jette ; University of Copenhagen, Nanoscience Center & Department of Chemistry Väli, Ronald; University Of Tartu Institute of Chemistry Härmas, Meelis; University Of Tartu Institute of Chemistry Lust, Enn; University of Tartu, Institute of Chemistry Von Bulow, Jon; Haldor Topsøe, NBU Jensen, Kirsten; Kobenhavns Universitet, Dept. of Chemistry Norby, Poul; Technical University of Denmark, Energy Conversion and Storage

Journal of Materials Chemistry A

ARTICLE

Following the In-plane Disorder of Sodiated Hard Carbon through *Operando* Total Scattering

0.211jReceived 00th January 2018,
Accepted 00th January 2018

DOI: 10.1039/x0xx00000x

www.rsc.org/

Jette K. Mathiesen,[a,b] Ronald Väli,[c] Meelis Härmas,[c] Enn Lust,[c] Jon Fold von Bülow, [d] Kirsten M. Ø. Jensen[a*] and Poul Norby [b*]

Successfully enabling a new battery technology, such as sodium-ion batteries, requires a thorough understanding of the functional properties of its building blocks. Knowing how the electrode materials behave upon operation is crucial to gain insight into how the battery technologies can be improved for optimal usage. Here we examine with X-ray total scattering and subsequent pair distribution function (PDF) analysis the structural response of hard carbon upon operation, which has been proposed as a possible electrode material for sodium ion batteries. PDF analysis reveals a clear correlation between the interplane and in-plane interatomic distances and the state of charge. The change in in-plane graphene behaviour corresponds to a reversible charge transfer between sodium and the antibonding orbitals in the upper π band of the graphene sheet, resulting in in-plane elongation and contraction upon cycling. As a result of the introduction of sodium into the structure upon discharge, the hard carbon structure is found to become increasingly disordered resulting in the initial structure not being able to fully recover upon desodiation. The more pronounced structural impact upon sodiation than seen in lithiated hard carbon suggests a larger electron transfer impact on the structure by influencing the π-orbitals of the neighboring, conjugated benzene rings. This means that the electron transfer cannot be described as a local electron transfer contribution as might be the case of lithium, but instead as a more delocalized contribution, in which the local structure of graphene experiences a larger change upon sodiation.

Introduction

Sodium-ion batteries (SIBs) have been recognized as a suitable candidate to meet the demands of low-cost energy-storage technologies. Although direct replacement of lithium-ion batteries (LIBs) with SIBs in current technologies seems intuitive due to the fundamental similarities, LIB electrode materials are not always suitable for sodium implementation and therefore new electrode materials capable of handling the larger sodium ion are needed. As a consequence of the high reactivity of pure metallic sodium in SIBs, sodium metal cannot be implemented as anode (negative electrode) in commercial cells. In addition, dendrite formation leads to limitations in battery safety and cycling efficiency [1]. In LIBs, this issue has been addressed by exchanging lithium metal with graphite as anode material. Graphite is an intercalation material, which denotes the reversible insertion process of a guest species into a host structure, and this process has been studied in detail in LIBs. Despite the chemical similarities to lithium, sodium has been found to intercalate poorly into graphite, unless co-intercalation of electrolyte solvents occurs [2]. The main explanation for this behaviour has been associated with the larger ionic radius of sodium [3]. However, the larger potassium ion has been found to intercalate in graphite with a resulting capacity of 244 mAh/g, which therefore shows the inconsistency of the current sodium-graphite intercalation model [4]. Liu et al. investigated the intercalation model through DFT-calculations and eventually came to the conclusion that the anomaly should be found in the higher formation energy of the sodium intercalated compound resulting from the weaker binding of sodium to the graphite substrate [5]. Additionally, Liu et al. concluded that for sodium to bind, a decrease of the strain energy must be obtained. In a layered material, straining is identified as both interlayer expansion and in-plane stretching to accommodate ion insertion. A decrease of strain energy can therefore be obtained if the material is pre-strained to obtain a larger interlayer spacing. However, a more desirable route is to utilize a material with an intrinsic larger interlayer spacing, which is the case of hard carbon [6]. Hard carbon, or non-graphitic carbon, consists of few layers of stacked or disordered graphene layers, which due to the non-periodicity results in an amorphous structure with a reported capacity of 300 mAh/g upon sodiation [7]. Several mechanisms for the sodiation process have previously been suggested, including intercalation between graphene layers, insertion between pores, as well as adsorption of sodium on defect sites [7, 8].

[a] Department of Chemistry and Nanoscience Center, University of Copenhagen, DK-2100 Copenhagen Ø.
[b] Department of Energy Conversion and Storage, Technical University of Denmark, DK-4000 Roskilde.
[c] Institute of Chemistry, University of Tartu, Ravila 14A, 50411, Tartu, Estonia.
[d] Haldor Topsoe A/S, DK-2800 Kgs. Lyngby.

†Electronic Supplementary Information (ESI) available: [details of any supplementary information available should be included here]. See DOI: 10.1039/x0xx00000x

Recently, a study combining *operando* ^{23}Na solid-state NMR and *ex situ* Pair Distribution Function (PDF) analysis of total scattering experiments proposes a two-stage model, in which the first step includes several mechanisms [9]. In the first step, ionic sodium ions are presumed to be localized near defects in the hard carbon structure. Larger interlayer distances resulting from presence of defects are assumed to allow sodium intercalation between graphene sheets with a larger interlayer spacing. ^{23}Na solid-state NMR results furthermore indicated an increased charge transfer to sodium ions at lower voltages, resulting in the sodium atoms becoming increasingly metallic in nature. Upon further intercalation, sodium clusters with coherence lengths of >10 Å are formed. The PDF data analysis indicated a significant degree of curvature of the graphene fragments [9]. However, to fully evaluate the structural influence of sodiation upon dynamic conditions, *operando* measurements must be performed. Here, we use *operando* X-ray total scattering with PDF analysis to follow in real time the structural changes that take place during charge and discharge of the hard carbon electrode. The PDF, denoted as *G(r)*, is the Fourier transform of the normalized reduced total scattering structure function, *F(Q)*, which utilizes the total scattering data obtained to high Q-values. This real-space function contains peaks at distances, *r*, representing pairs of atoms in the structure, where sharp peaks indicate a well-defined structure of the hard carbon material, resulting in a histogram of interatomic distances. Additionally, the intensities of the peaks are related to the relative abundance of each atom-atom distance. Consequently, the PDF analysis provides an intuitive tool to study the local atomic structure of a material. To overcome the challenges related to the low scattering power of carbon and sodium, we use a custom-built low-background *operando* setup for achieving useful data for PDF analysis rather than conventional pouch or coin cell-like cells for synchrotron *operando* experiments. Our custom-made capillary-based battery cell allows selective scattering from only the electrode material of interest [10, 11]. Due to the configuration of the cell, where the X-ray beam only sees the capillary, electrolyte and the active material, the contribution to the background only originates from the capillary and the electrolyte, which is easily subtracted from the total scattering intensity for subsequent PDF analysis (Figure 1). The setup ensures that the X-rays reach the active material without having to penetrate multiple absorbing and diffracting layers, such as X-ray windows, anode and separator, which would result in difficulties in isolating the signal from the weakly scattering active material. In fact, both electrodes can be selectively analyzed during operation, but in this study the focus is directed towards the hard carbon electrode operating in a half-cell versus metallic sodium. From the PDF data, it is observed that clear interlayer and in-plane changes of the graphene layer as well as increasing disordered behaviour of the hard carbon structure upon discharge occurs, indicating that sodium ion insertion in hard carbon resembles the behaviour of ion intercalation in graphite.

Experimental Details

Synthesis of hard carbon. The glucose-derived hard carbon (GDHC) was prepared in three steps. Hydrothermal carbonization of 2 M D-(+)-glucose solution in H_2O (200 ml) was carried out in a high-pressure reactor (Büchi limbo, vessel volume 285 ml) at 200 °C for 24 hours. Thereafter, the carbonaceous material was collected and washed several times with Milli-Q$^+$ water (Milli-Q$^+$, 18.2 MΩ cm, Millipore), and dried overnight in a vacuum oven (Vaciotem-TV) at 120 °C and 50 mbar. The dried carbonaceous material was then pyrolysed in a quartz stationary bed reactor at 1100 °C under Ar flow for 2 h using heating ramp rate of 10 °C min^{-1}. Finally, the carbon material was treated with H_2 (purity 99.9999%) at 800 °C for 2 hours to reduce surface functional groups [12].

Electrode preparation. The capillary-based half-cell consists of two flat current collectors of aluminium and copper (0.7mm wide 0.3mm thick) coated with hard carbon (100-200 µm layer) and sodium metal, respectively. First, a hard carbon slurry was prepared in a fume hood by mixing 80 w% hard carbon, 15 w% polyvinylidene fluoride (PVDF) and 5 w% Super P in N-methyl-2-pyrrolidone (NMP), which was stirred for 72 hours. The aluminium wire was coated 2-3 times with the slurry using a spatula with subsequent drying for 30 min at 100° C after each application. After coating and drying, the coated hard carbon electrode was cut to achieve a length of approx. 2 mm. The resulting electrodes were transferred to the glovebox and dried in a vacuum oven overnight at 80 °C to remove residual water. The counter electrode consisted of a copper wire current collector, which was coated with a thin sodium metal layer.

Cell assembly in glovebox. To obtain a constant distance and preventing contact between the electrodes, the electrode wires were fixed with UV-glue on a plastic spacer. The separated wires were placed in a rectangular boron silicate capillary (Hilgenberg) with an outer diameter of 4.2 × 1.25 mm and wall thickness of 0.125 mm, in which they were fixed by epoxy glue (Loctite 9492) and dried overnight at room temperature. The capillary was filled with 0.5 M $NaClO_4$ electrolyte (in propylene carbonate with 2 vol.% FEC). Finally, it was sealed by firstly applying a small amount of silicone grease at the capillary opening followed by two-component epoxy glue. The schematics of the resulting capillary-based sodium ion half-cell is displayed in Figure 1.

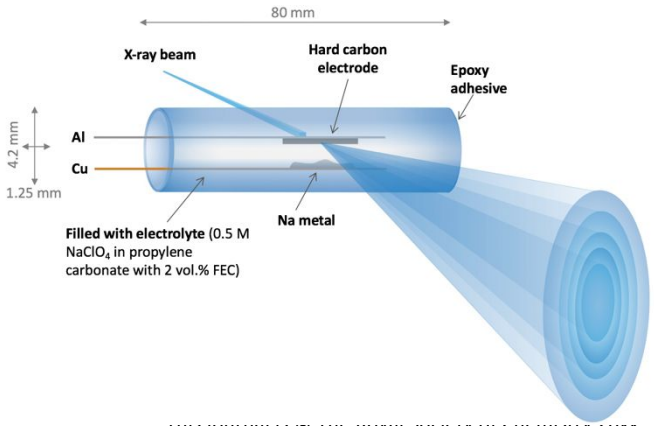

Figure 1 A sketch of the capillary-based battery cell.

Setup for *operando* synchrotron total scattering. The mounting of the capillary-based half-cell is illustrated in Figure S1 (ESI†). The half-cell was placed in an insulating frame and mounted horizontally on a goniometer head. The current collectors were connected to a potentiostat (8-channel MACCOR® battery cycler) to charge and discharge the half-cell at a C-rate of approximately C/10 in a potential window of 0.01-2.1 V with 5 minutes of open-circuit voltage (OCV) between the modes. Total scattering data were collected in transmission geometry using a Perkin-Elmer flat panel detector with a pixel size of 200x200 µm. A wavelength of 0.2114 Å was used and the X-ray beam was defined by slits: vertically 150 µm and horizontally of 500 µm. A CeO_2 standard was used to calibrate the sample-to-detector distance. Total scattering data were collected by first measuring 4.5 minutes at a position on the hard carbon, where the best scattering signal from the electrode was found (Position 1, Table S1 (ESI†)) with a detector distance of 18 cm. Afterwards, the capillary was moved in the vertical plane, so that data were collected at a point closer to the electrolyte, where a new frame was measured for 4.5 minutes (Position 2). The sample was then moved vertically 300 µm to collect data from the electrolyte for background correction (Position 3). The sequence of measurements, which made it possible to continuously subtract a representative electrolyte state, is tabulated in Table S1 (ESI†). In total, this data collection sequence took 30 minutes, which was then continuously executed during operation of the half-cell. The data were integrated using *Fit2D* [13] and the PDFs were obtained from the initial *operando* total scattering data by utilizing PDFGetX3 [14] with subsequent background subtraction of the background data measured in Position 3 [13, 14].

Characterization with high-resolution transmission electron microscopy. High-resolution transmission electron microscopy (HR-TEM) data were collected using a Tecnai 12 instrument operated at an accelerating voltage of 120 kV. The TEM specimens were prepared from ultrasonic dispersions of the corresponding samples in ethanol. One drop of each suspension was deposited onto a copper grid covered with a holey carbon film.

Results and Discussion

We first consider the scattering data in Q-space measured at Position 1. Figure 2 shows *operando* intensity data, *I(Q)*, from the 1st discharge of the half-cell, where the colour code identifies the position in the discharge curve. The large majority of the scattering signal arises from the capillary and electrolyte, as presented in the enhanced view of Figure 2, and owing to the non-periodic nature of the hard carbon material, only very broad and weak scattering peaks are present in the scattering pattern. As a consequence, only limited structural information can be obtained from the scattering patterns with traditional crystallographic methods. However, besides the dominating background scattering peak at Q=1.8 $Å^{-1}$, in which the 002 reflection is hidden, a broad diffraction peak seems to develop upon sodiation at Q=3.7 $Å^{-1}$, corresponding to the 004 diffraction peak from the graphite structure. Additionally, the diffraction peak appears to move towards lower scattering angles, indicating that the graphene interlayer distance expands in the hard carbon structure upon sodiation. A new peak seems to develop upon sodiation at Q=2.7 $Å^{-1}$ (indicated by the black arrow), which might originate from to sodium interaction in the structure, since the diffraction peak cannot be described by a pure graphite model. As for the in-plane diffraction peaks of graphene identified as the 010 and 110 reflections, the analysis of the structural changes taking place are limited by the broad nature of the peaks. Consequently, to extract information from these weak reflections, we turn to PDF analysis of the X-ray total scattering data in real space.

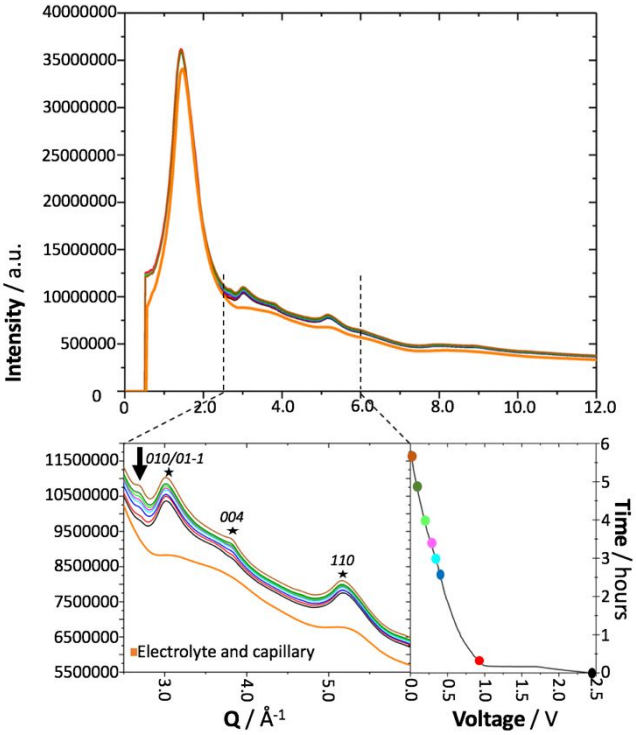

Figure 2 *Operando* total scattering data of hard carbon upon sodiation relating the electrochemical state of discharge and the changes in reciprocal space.

The PDF obtained from the hard carbon electrode before cycling is shown in Figure 3. The PDF clearly illustrates the limited structural coherence in the hard carbon material as no long-range order peaks are seen above 25 Å. However, the sample has very well-defined local range order as seen from the sharp low *r*-range peaks, corresponding to the C-C correlations indicated in the insert structure. The loss of long-range order has been proposed to be caused by termination of carbon fragment sheets by either hydrogen atoms or a functionalized group or by the presence of non-hexagonal rings causing sheet curvature [15].

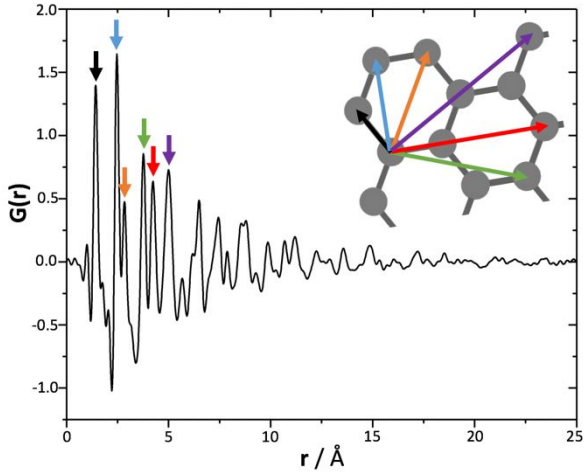

Figure 3 PDF of pristine hard carbon in the full r-range revealing absence of long-range order.

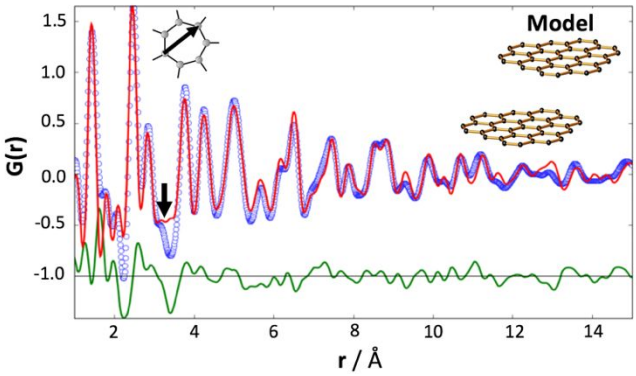

Figure 4 Refinement of first scan of hard carbon sodiation in the r-range from 1-15 Å. Inset shows the ex-tended graphite model used for the refinement and the seven-membered ring related to the peak at 3.2 Å.

The Structure of Hard Carbon

To be able to quantify the structural changes of the hard carbon, a model was developed describing the atomic arrangement. The model is characterized as an altered, extended graphite structure, which can be assigned as an intermediate between the periodic 2H graphite structure and a single graphene layer, where a structural model is shown in the inset of Figure 4 [9, 16]. The modification from bulk graphite is introduced through an increased *c*-parameter (7.0 Å) from that of the pristine 2H structure (6.70 Å in graphite, [17]) and increased atomic displacements parameters in the *c*-direction, assisting to describe the lower density of the hard carbon compared to graphite (1.52 g/cm^3 compared to graphite values of 2.26 g/cm^3) [9, 18], as well as the presence of turbostratic disorder suggested by Bommier et al [8]. Real-space least-squares refinement of the pristine hard carbon was performed against experimental PDF data in the *r*-range from 1-15 Å. A representative refinement is shown in Figure 4. As seen in Figure 4, the presented model agrees well with previous studies, in which the PDF of the hard carbon is primarily dominated by in-plane carbon-carbon interaction and not significantly by the sheet-sheet correlation [16]. Specifically, as observed in Figure 4, the model resembles the experimental PDF very well above 4 Å. However, at lower *r*, especially at 3.2 Å, the model has difficulties fitting the features of the experimental PDF. The observed peak is consistent with previous *ex situ* PDF studies on the presence of seven-membered carbon rings with non-hexagonally bonded carbon rings [19].

Structural Changes upon Cycling

To follow the structural changes occurring within the hard carbon material upon operation, *operando* total scattering data were obtained. The resulting plot of *operando* PDFs upon discharge is presented in Figure 5. In the range shown in the figure, the PDF is mainly dominated by the C-C correlations in a single graphene sheet, as indicated by the marked distances in Figure 3. As the concentration of sodium in the hard carbon material increases during sodiation, denoting discharge of the half-cell, it is clearly illustrated that the whole graphene layer structure, including the closest C-C bond distance in the benzene ring, becomes more disordered upon sodiation as peak broadening is seen (Figure 5, below). Similar broadening effects were observed from *ex situ* measurements of hard carbon samples obtained from different stages of the discharge process in a pouch half-cell (Figure S2 ESI†). Interestingly, the intensity of the peak seen in the experimental PDF at 3.2 Å (indicated by the arrow) increases upon sodiation, which would indicate an increase in the presence of seven-membered rings, and therefore introduction of bond breakage and associated disorder [19]. However, another likely more probable explanation might be related to broadening of the surrounding peaks, smearing out the electron density and therefore resulting in intensity increase around the peak centre. Finally, as seen in the *operando* PDFs upon subsequent discharge-charge cycles, the peaks representing the C-C correlated distances never fully reach the features of the fully desodiated state found in the initial hard carbon material, as they still contain a significant degree of disorder. In Figure 5, this is especially visible at 1.42 Å, where the sharpness of the initial peak is never recovered. This behaviour agrees with the irreversible loss of capacity seen in the galvanostatic cycling measurement (Figure S3 ESI†). Consequently, the irreversible capacity loss and further capacity fading might indicate that the sodium inserted in the

material becomes trapped at hindered sites within the porous material, resulting in less sodium being available for extraction upon subsequent charging cycles. However, due to the cell configuration, where an increased distance between the electrode materials is implemented to selectively examining the active material, fully separating structural and cell related contributions to the capacity loss is limited in the given study.

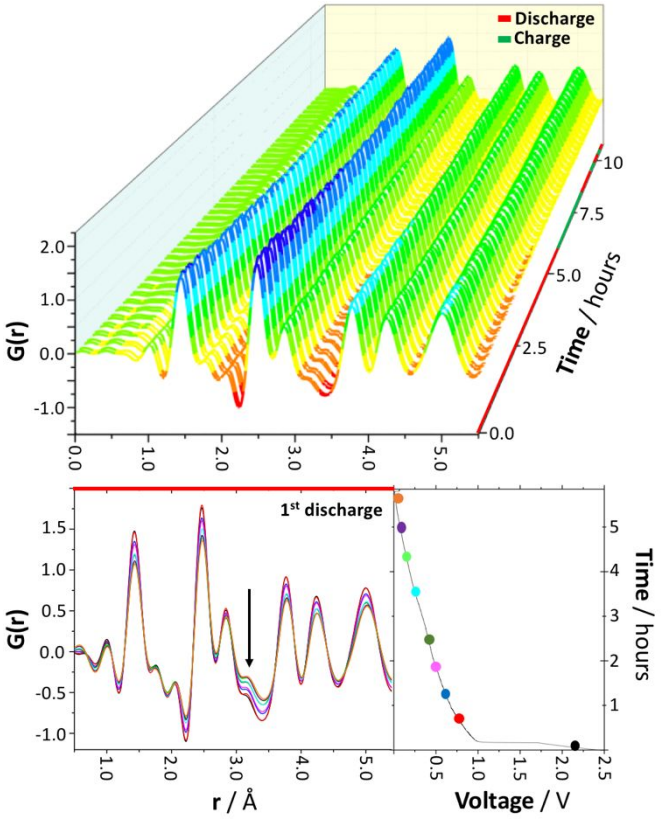

Figure 5 *Operando* study of the dynamical evolution of the graphene structure upon sodiation. *Top) Operando* PDF data in the *r*-range representing the graphene correlation structure as a function of electrochemical state (indicated in the bar diagram on the right of the figure). *Below*) Selected *operando* PDFs of the first discharge relating the electrochemical state of discharge and the changes in real space.

Quantitative analysis of the *operando* PDFs was done employing the presented extended graphite model, which was refined to the time-resolved data. Figure 6 shows the refined *a* and *c* parameters as a function of time, representing the discharge/charge state. As observed in Figure 6, both *a* and *c* increase upon sodiation. The increase in *c*-parameter indicates intercalation, where sodium inserts between correlated or nearly aligned graphene sheets causing the interlayer to expand. Consequently, as charging is initiated with an associated de-intercalating behaviour, the *c*-parameter is found to decrease. In addition, the expansion of the in-plane graphene cell parameters, corresponding to the C-C bonds in the graphene layers, has previously been observed in lithiated graphite [20], potassium intercalation in graphite [21], and studied through theoretical *ab initio* calculations [22]. The bond-length increase in the graphite intercalated systems was found to be associated with an electron transfer from the σ orbitals of the intercalated ion to the antibonding orbitals in the upper π band of the graphitic region between the intercalate layers, which is consistent with the C-C bond reduction and resulting elongation found in the graphene sheets.

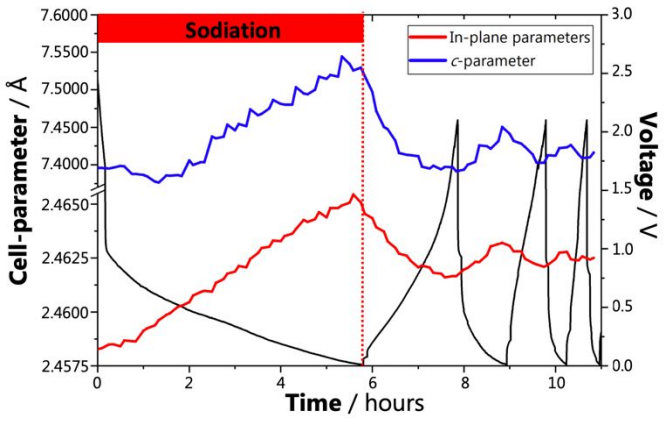

Figure 6 Refinement of cell parameters of the hard carbon structure upon sodiation as a function of the electrochemical cycling state. The electrochemical state of the half-cell is indicated as the black curve with corresponding cell voltage on the right of the figure. The red bar diagram indicates when the first sodiation process occurs.

The quality of the fit using the developed altered graphite model was improved by modelling independently the PDF in two r-ranges: the low-*r* range from 1-5 Å and the high-*r* range from 4.5-10 Å, where the refinement fit is presented in Figure S4 ESI†. The refined *a* parameter for the 1-5 Å range (blue) and 4.5-10 Å range (red) is shown in Figure 7A along with the parameters obtained from the fit from the entire *r*-range from 1-15 Å (black). Fitting in the local *r*-range gives significantly larger in-plane parameters than when fitting to the longer-range order peaks, indicating that one single model cannot describe the full structure. The behaviour can be understood in terms of curvature of the graphene sheets as also observed by Stratford et al [9]. Comparing a planar graphene sheet and a curved structure, the resulting distances between carbon atoms at high-r will significantly differ in the two models. In a curved structural model, the result of moving into the high-r region results in carbon atoms being closer together than described by the planar model, which is schematically illustrated in Figure 7C. The effect is seen throughout the cycling process of the half-cell and appears intrinsic to the hard carbon structure and not affected by the sodiation. Additionally, the intrinsic behaviour of curved sheets was further supported by HR-TEM, in which more isolated graphene sheets were found to exhibit pronounced curvature, whereas less pronounced curvature was observed for multilayered graphene sheets as illustrated in Figure 7B.

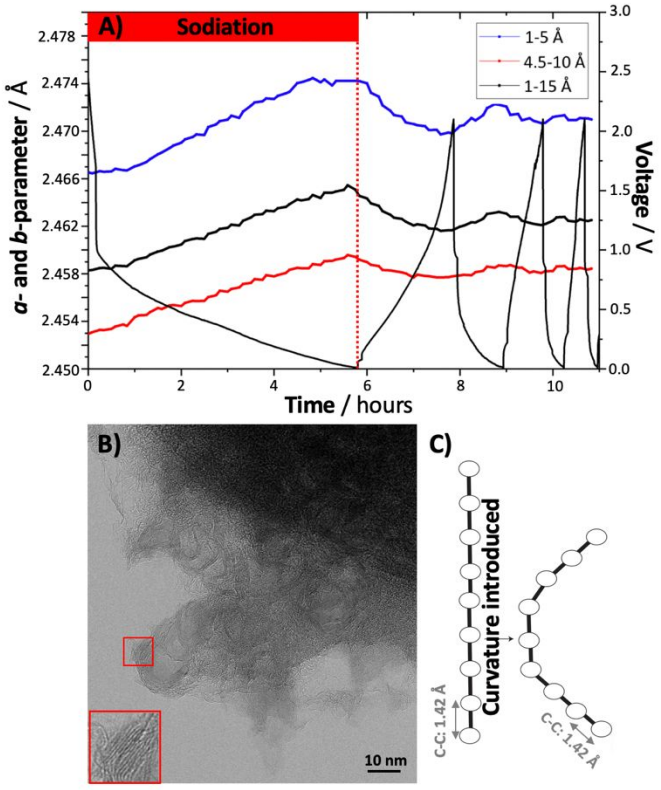

Figure 7 *A*) Refinement of cell parameters *a* and *b* of the hard carbon structure upon sodiation in the three r-ranges of refinement as a function of the electrochemical cycling state. The electrochemical state of the half-cell is indicated as the black curve with corresponding cell voltage on the right of the figure. The red bar diagram indicates when the first sodiation process occurs. *B)* HR-TEM of hard carbon illustrating curvature. *C*) Schematic illustrating how the effect of curvature influences the *r*-ranges utilized in the refinement.

The atomic displacement parameters (ADPs) describing atomic motion in and between the graphene layers, U_{11}/U_{12} and U_{33}, respectively, are used to quantify the degree of disorder present. Figure 8 shows the refined ADP values obtained from refinements of the high-*r* (4.5-10 Å) data as a function of time and electrochemical state of charge. The in-plane ADPs (U_{11} and U_{22}) refined in the long-range order regime are less affected by the cycling process; and as seen in the pristine hard carbon PDF (Figure 3), the structure is already intrinsically dominated by short-range order in the graphene sheet, whereas long-range order is significantly weaker due to either the presence of curvature or termination of graphene fragments in the material as discussed previously. Therefore, the induced disorder in the structure upon sodiation does not affect the intrinsic long-range structure, as a significant degree of disorder is already present. For the ADPs describing the interlayer disorder (U_{33}), increasing behaviour is displayed following the electrochemical cycling state. The increasing displacement parameter in the high-*r* region upon sodiation suggests either that the electron distribution from the graphene layers becomes delocalized or that the model is not sufficient in describing the disordered structure.

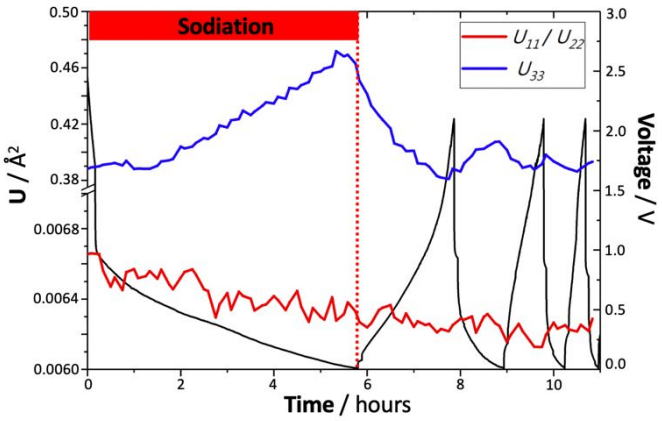

Figure 8 Atomic displacement parameters (ADPs) of hard carbon upon sodiation from high-*r* refinement (4.5-10 Å). The red curve displays in-plane ADPs, U_{11}/U_{22}, whereas the black curve displays the interlayer ADPs, U_{33}. The electrochemical state of the half-cell is indicated as the black curve with corresponding cell voltage on the right of the figure. The red bar diagram indicates when the first sodiation process occurs. The red bar diagram indicates when the first sodiation process occurs.

As discussed previously, one of the proposed mechanisms of sodiation involved sodium binding to carbon at either termination or defect sites with an additional formation of metallic sodium clusters. For this to occur, a correlation corresponding to a sodium-sodium or sodium-carbon interaction in the structure should be revealed upon sodiation. A method to reveal such interactions developing is through differential PDF (d-PDF). d-PDF can be implemented, since assigning the individual peaks in the PDF to specific pair correlations might not always be a straightforward procedure [23]. The approach achieved through this implementation isolates correlations arising from the modification of the structure by sodiation. Consequently, the direct subtraction performed between the state with no sodium present (the fully charged half-cell) and the most sodiated state (discharged half-cell) directly provides peaks, where sodium interactions can be identified as the carbon signal is subtracted from the resulting data. As observed in the d-PDF, no significant sodium-sodium interactions were revealed in the local structure (Figure S5 ESI†), illustrated by the absence of the features at 3.7 Å, 7 Å and 9.5 Å, corresponding to sodium metal and cluster formation [9]. However, the absence of metallic sodium in this experiment should not be assumed to indicate that the formation of metallic sodium and clusters will never occur. It could simply be that the state of metal formation has not yet been reached, which is in agreement with the low capacity seen in the galvanostatic cycling measurement (Figure S3 ESI†). Furthermore, the observed increased disorder of the graphene structure coincides with the first peak associated with sodium metal (3.7 Å). Therefore, the features introduced in the structure upon sodiation could be a combination of both the structural changes of hard

carbon, sodium-carbon interactions and sodium metal and cluster formation.

The Lithium Analogue

To further our understanding of how ion insertion in hard carbon can be described, a lithium analogue experiment was performed *operando* with identical electrochemical conditions. The galvanostatic discharge of the capillary-based half-cell showed a similar discharge capacity of 171 mAh/g (Figure S6 ESI†), revealing that the half-cell again is associated with a significant capacity loss as only 68% of the theoretical discharge capacity is obtained [24, 25]. The PDFs from lithiation of hard carbon display the same broadening behaviour, indicating induced disorder in the structure as observed for hard carbon sodiation (Figure 9). Furthermore, the feature at 3.2 Å (indicated by the inserted arrow) also appears upon lithiation, which indicates that the peak is not related to a sodium-carbon pair that could appear upon sodium insertion. Instead, it possibly relates to the previously proposed assumption of seven-membered rings in the structure and additional increase attributed to delocalization of electron density from induced disorder causing broadening of the surrounding peaks, as seen for sodiated hard carbon [15]. In addition, a corresponding lithium-carbon peak would be much less intense due to the low scattering power of lithium. Consequently, this indicates that the insertion mechanism of lithium and sodium in hard carbon are similar.

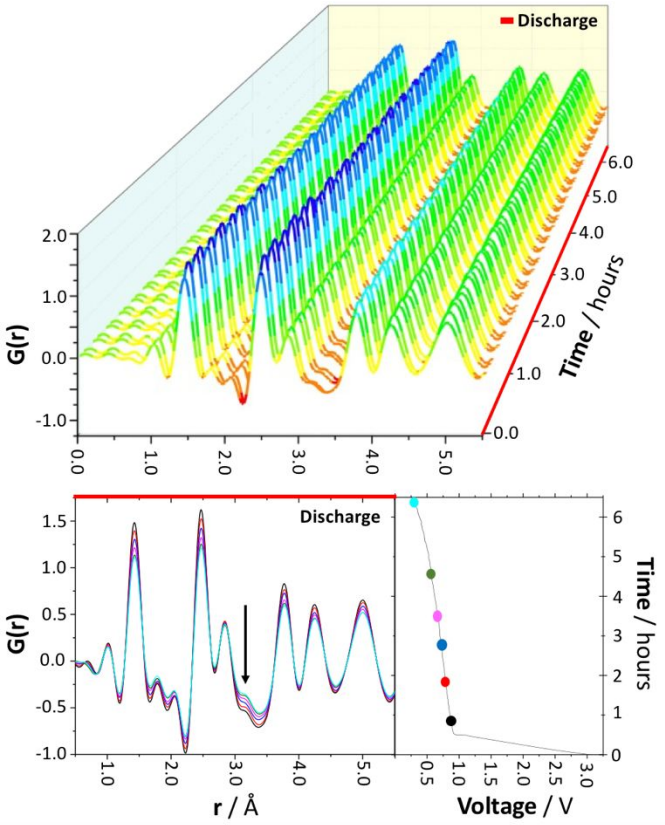

Figure 9 *Operando* study of the dynamical evolution of the graphene structure upon lithiation. *Top) Operando* PDF data in the *r*-range representing the graphene correlation structure as a function of electrochemical state (indicated in the bar diagram on the right of the figure). *Below*) Selected *operando* PDFs of the first discharge relating the electrochemical state of discharge and the changes in real space.

Real-space least-squares refinement was also performed against experimental lithium insertion PDF data with the same model as presented for sodium (see Figure S7 ESI† for refinement of all *r*-ranges). As identified in the refinement, similar expansion of the in-plane graphene parameters upon lithiation is observed as revealed upon sodiation (Figure S8 ESI†). However, the *c*-parameter does not appear to follow the same rate of increasing behaviour as observed upon sodiation. This might be attributed to the smaller size of lithium causing a less hindered insertion and extraction of lithium from the structure with a less pronounced impact on the interlayer spacing. However, as proposed by Liu et al based on DFT calculations, the intrinsically very similar ions of lithium and sodium display different insertion behaviour in graphite due to the weaker binding of sodium to the substrate [5]. Therefore, to further elucidate why such differences are present and if the lower rate of interlayer expansion might be related to this behaviour, the in-plane response to the ion insertion procedure was investigated by comparing the percentage change of the in-plane cell parameters from the initial pristine model. The calculation was performed by subtracting the initial value of the in-plane parameter from each subsequent in-plane parameter provided from the refinement, followed by conversion to a percentage change. As illustrated in Figure 10 (black curve), the insertion of sodium in the hard carbon material results in a change of in-plane cell parameters approximately 60 % larger than for lithium insertion. Considering the ionic sizes of sodium and lithium (116 pm and 90 pm, respectively [26]), the 20 % larger sodium ion would correspondingly result in a larger expansion. However, this insertion model does not consider electron charge transfer to the graphene sheet. The in-plane expansion would therefore be a combination of both size-accommodating interaction and charge transfer causing reduction. Furthermore, the increased expansion of the graphene layer upon sodiation suggests that the ion insertion behaviour might not be fully described through the previously mentioned local electron transfer model to the antibonding π-orbitals of the graphene layers. As the larger sodium ion is inserted in hard carbon, the larger expansion could suggest a larger electron transfer impact on the structure by influencing the π-orbitals of the neighbouring, conjugated benzene rings. This means that the electron transfer cannot be described as a local electron transfer contribution as might be the case of lithium, but instead as a more delocalized contribution.

Consequently, this means that as hard carbon, to some extent, is found to resemble the behaviour of ion intercalation in graphite upon both sodiation and lithiation, i.e. C-C bond elongation and interlayer expansion, it is proposed that the mechanism of ion insertion most likely follows an intercalating procedure. In this process, the sodium or lithium ions will intercalate between graphene layers resulting in interlayer expansion, following a charge transfer from the ions to the graphene layer with subsequent charge delocalization, causing

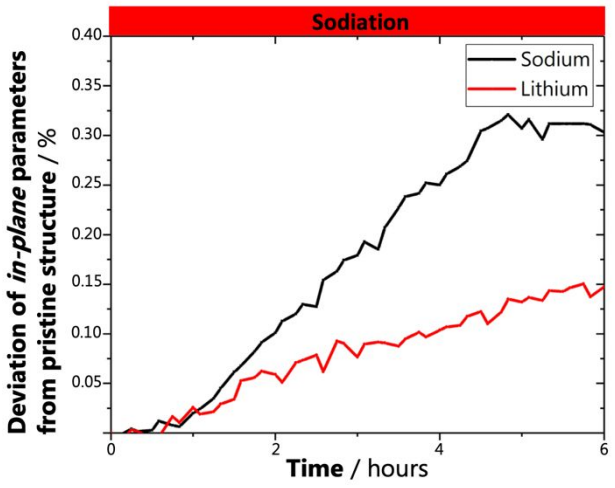

Figure 10 The difference in *in-plane* behaviour upon ion insertion. The figure illustrates the relative change of the *in-plane* cell parameters upon ion insertion. The black curve displays the sodiation response, whereas the red curve provides the lithiation response. The red bar diagram indicates when the first sodiation process occurs.

a C-C bond length reduction. The structural impact is more pronounced upon intercalation of the larger sodium ion as compared to lithiation, which is suggested to relate to an electron transfer contribution to the neighbouring, conjugated hexagonally coordinated carbon rings next to where the sodium is positioned in the structure as illustrated in Figure 11. The previously proposed mechanism of metallic sodium and coordination at defect or termination sites are however not directly observed in the given experiment. However, these mechanisms might occur in the hard carbon, but at a later stage in the sodiation process, which in this experiment is limited by the low capacity obtained.

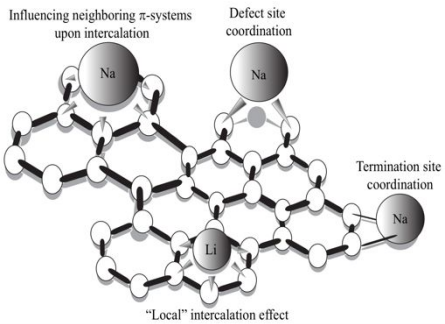

Figure 11 Mechanisms of ion insertion and the corresponding structural impact on the graphene layer.

Conclusion

To elucidate the sodiation mechanism of hard carbon, *ex situ* and *operando* synchrotron X-ray radiation total scattering experiments were performed at P02, Petra III, Deutsches Elektronen-Synchrotron, and 11-ID-B, APS, Argonne National Laboratory, respectively. From the total scattering measurements, it was possible to index the graphene C-C correlation distances using a disordered graphite model with only short-range order. Upon sodiation, the peaks became broadened indicating increased disorder. The refinement of the obtained PDF data revealed that inter- and intralayer expansions appear upon sodiation, suggesting the possibility for intercalating behaviour. The expanding behaviour corresponds to a reversible charge transfer between the σ-orbitals of sodium and the antibonding orbitals in the upper π-band of the graphene sheet resulting in bond reduction. Consequently, in-plane elongation and contraction are observed upon discharge and charge, respectively. However, the data also revealed that the hard carbon structure becomes increasingly disordered upon discharge, in which the initial structure is never fully recovered consistent with the observed irreversible capacity loss. Indications of sheet curvature was also observed from the refinement of in-plane cell parameters, through an overestimation of high-*r* data fitting compared to low-*r* fitting. This suggests that carbon atoms at higher r will be separated by a shorter distance compared to a planar graphene sheet model describing the low-*r* behaviour.

As an attempt to disentangle overlapping contributions from the C-C correlation distances and possible sodium-sodium or sodium-carbon bonds, an *operando* experiment of lithiated hard carbon was performed. Intercalation behaviour was also clearly identified with expanding cell parameters, but at a much lower rate than as seen upon sodiation. Furthermore, in-plane broadening behaviour was observed for both half-cell systems, corresponding to a partial reduction of the graphene sheets inducing a C-C bond length distribution dependent on the degree of sodiation. However, the sodiation process is again found to cause a more significant influence on the graphene sheet structure. The more pronounced structural impact upon sodiation suggests a larger electron transfer impact on the structure by influencing the π-orbitals of the neighbouring, conjugated benzene rings. This means that the electron transfer cannot be described as a local electron transfer contribution as might be the case with lithium, but instead as a more delocalized contribution, in which the local structure of graphene experiences a larger change upon sodiation.

Conflicts of interest

There are no conflicts to declare.

Acknowledgements

The authors would like to acknowledge the staff of beamline 11-ID-B at APS and P02.1 at PETRA III (DESY) for experimental assistance. Use of the Advanced Photon Source, an Office of Science User Facility operated for the U.S. Department of Energy (DOE) Office of Science by Argonne National Laboratory, was supported by the U.S. DOE under Contract No. DE-AC02-06CH11357. The Danish Research Council is acknowledged for covering travel expenses in relation to the synchrotron experiment (DanScatt). Estonian Research Council and European Regional Development Fund are acknowledged for partially supporting this work through Institutional Research Grant IUT20-13 and Centre of Excellence project 2014-2020.4.01.15-0011, respectively.

References

1 Ellis, B. L. and Nazar, L. F., *Current Opinion in Solid State and Materials Science*, 2012, **16**, 168-177.
2 Jache, B. and Adelhelm, P., *Angew. Chem Int. Ed.*, 2014, **53**, 10169-10173.
3 Y. Wen, K. He, Y. Zhu, F. Han, Y. Xu, I. Matsuda and C. Wang, *Nature Communications*, 2014, **5**, 4033.
4 S. Komaba, T. Hasegawa, M. Dahbi and K. Kubota, *Electrochemistry Communications*, 2015, **60**, 172-175.
5 Y. Liu, B. V. Merinov, and W. A. Goddard, *Proceedings of the National Academy of Sciences*, 2016, **113**, 3735-3739.
6 E. Irisarri, A. Ponrouch and M. R. Palacin, *J. Electrochem. Soc.,* 2015, **162**, A2476-A2482.
7 D. A. Stevens and J. R. Dahn, Journal of the Electrochemical Society, 2000, **147**, 1271-1273.
8 C. Bommier, T. W. Surta, M. Dolgos and X. Ji, *Nano letters*, 2015, **15**, 5888-5892.
9 J. M. Stratford, P. K. Allan, O. Pecher, P. A. Chater, and C. P. Grey, *Chem. Commun.*, 2016, **52**, 12430-12433.
10 R. Johnsen and P. Norby, *J. Appl. Cryst.*, 2013, **46**, 1537-1543.
11 Christiansen, A. S., Johnsen, R. E., Norby, P., Frandsen, C., Mørup, S., Jensen, S.H., Hansen, K.K. & Holtappels, P., *J. Electrochem. Soc*., 2015, **162**, A531-A537.
12 R. Väli, A. Jänes, T. Thomberg, and E. Lust, *Journal of The Electrochemical Society*, 2016, **163**, A1619-A1626.
13 A. P. Hammersley, *Journal of Applied Crystallography*, 2016, **49**, 646-652.
14 P. Juhás, T. Davis, C. L. Farrow, and S. J. Billinge, *Journal of applied Crystallography*, 2013, **46**, 560-566.
15 P. J. Harris, Z. Liu and K. Suenaga, *Journal of Physics: Condensed Matter*, 2008, **20**, 362201.
16 V. Petkov, R. G. Difrancesco, S. J. L. Billinge, M. Acharya and H. C. Foley, *Philosophical Magazine B*, 1999, **79**, 1519-1530.
17 A. H. Palser, *Physical Chemistry Chemical Physics*, 1999, **1**, 4459-4464.
18 M. B. Dowell, and R. A. Howard, *Carbon*, 1986, **24**, 311-323.
19 A. C. Forse, C. Merlet, P. K. Allan, E. K. Humphreys, J. M. Griffin, M. Aslan, M. Ziegler, V. Presser, Y. Gogotsi and C. P. Grey, *Chemistry of Materials*, 2015, **27**, 6848-6857.
20 Zou, J., Sole, C., Drewett, N. E., Velický, M., & Hardwick, L., *The journal of physical chemistry letters*, 2016, **7**, 4291-4296.
21 D. E. Nixon and G. S. Parry, *J. Phys. C (Solid St. Phys.)*, 1969, **2**, 1732-1741.
22 C. T. Chan, W. A. Kamitakahara and K. M. Ho, *Phys. Rev. Lett.*, 1987, **58**, 1528-1531.
23 K. W. Chapman, P. J. Chupas, & C. J. Kepert, *Journal of the American Chemical Society*, 2005, **127**, 11232-11233.
24 R. Väli, A. Jänes, T. Thomberg and E. Lust, *Electrochimica Acta*, 2017, **253**, 536-544.
25 R. Väli, A. Jänes and E. Lust, *Journal of The Electrochemical Society,* 2017, **164**, E3429-E3437.
26 R. D. Shannon, *Acta crystallographica section A: crystal physics, diffraction, theoretical and general crystallography*, 1976, **32**(5), 751-767.